Title: Measuring the atomic composition of planetary building blocks.

Authors: Melissa K. McClure,[1]* Carsten Dominik[1].

Affiliations:

[1]Anton Pannekoek Institute for Astronomy, University of Amsterdam, Science Park 904, 1098 XH Amsterdam, Netherlands.

*Correspondence to: Email: melissa.k.mcclure@gmail.com

Abstract:

Volatile molecules are critical to habitability, yet difficult to observe directly at the optically thick midplanes of protoplanetary disks, where planets form. We present a new technique to measure indirectly the bulk atomic composition and distribution of solids that have been removed from the gas accreting onto the young star TW Hydrae. Our results suggest that disk gaps and planetesimal formation in TW Hya efficiently prevent radial drift and effectively block replenishment of the inner disk solids from ice reservoirs. Volatile-enhancement of giant planet atmospheres cannot be explained by primary accretion of this gas. Half of the missing oxygen is locked in silicates inside the snowline, while carbon is predominantly locked in organics beyond the CO snowline, leaving terrestrial planet-forming region solids both 'dry' and carbon-poor. Earth's depletion of carbon could be common amongst terrestrial exoplanets.

One Sentence Summary: Dry, carbon-poor terrestrial planets, like Earth, could be common.

Main Text: The variety of masses, radii, and semi-major axes of observed exoplanets indicates a diversity of compositions. A key goal of exoplanet research is to use these compositions to trace the formation location and timing of planets, which are built by accretion of gas and solids. Abundance ratios between volatile and refractory elements, e.g. C/O and C/Si, are used to characterize exoplanet atmospheric compositions *(1)* and solar system solid bodies *(2)*. Despite high solar abundances and enhancement in gas giant atmospheres, carbon, oxygen, and nitrogen are depleted relative to silicon on Earth and some classes of asteroids *(2-4)*. The fraction of each element in refractory organics versus volatile ices may influence these trends. Sublimation of ices could enhance gaseous abundances at the expense of solids *(5, 6)*, and additional mechanisms may exist to destroy refractory organic grains in the inner regions of protoplanetary disks while retaining silicon-rich dust *(7)*. Radial transport of fresh solids from the cold outer disk could renew the organics in the terrestrial planet forming region, and it may be, e.g., that the low C/Si ratios in solar system bodies are simply a consequence of Jupiter segregating the inner solar nebula, rather than a universal destruction mechanism *(8)*. However, the midplane distribution of ices and organics in protoplanetary disks is not yet observationally well-determined, due to dust and gas optical depth effects.

For one nearby disk, TW Hydrae (TW Hya), the presence of a midplane ice reservoir is inferred from recently measured gas depletions of CO (~100x) and H_2O (~800x), relative to the ISM value *(9-13)*. These 'missing' volatiles are thought to be frozen on icy midplane dust particles, which have grown so large that they no longer vertically circulate into the region where the ice can be photodesorbed. Dust evolution models predict enhanced gaseous C/H and O/H in this region *(5, 6)*, in contrast with TW Hya's observed behavior *(14)*, suggesting that either CO ice is chemically processed into a more refractory carbon carrier or that dust radial drift is inefficient due to dust trapping or planetesimal formation. Measurements of the bulk elemental abundances in the gas being accreted onto the star should distinguish between chemical processing or dust locking, but it is difficult to isolate the emission of the innermost, dust-free region of protoplanetary disks from contributions by the stellar photosphere and dust sublimation rim. Recently, this inner gas was directly detected in disks through near-infrared atomic carbon emission lines, allowing a neutral carbon column density measurement *(15)*. That work provided a conversion of n_C to C/H, but did not measure n_H or other critical elements, e.g. O or Si, which could provide a similar assessment for water.

Here we use time differential spectroscopy of hydrogen lines in TW Hya to measure n_H directly [see methods and materials]. By fitting emission line flux ratios in a radial slab using the photoionization and chemistry code Cloudy *(16)*, we derive abundances of several major atomic species relative to hydrogen. We then extract the bulk elemental abundances of solids left behind, relative to silicon, and compare both of these results with elemental abundances of solar system bodies to determine TW Hya's refractory fraction and locking efficiency.

We vary n_H of the slab model to fit the observed Paβ/Paγ flux ratio in the residuals of the 2013-2010b and 2010b-2010a time differential spectroscopy. TW Hya experienced a 0.25 dex increase in overall gas number density between the 2010b and 2013 epoch observations, suggesting accretion of a local gas overdensity. Taking the 2013 value of n_H, we fit X/H to the flux ratios between Paγ and the C, S, O, and Ca lines detected in the observed spectrum. Strong lines of N, K, Na, Mg, Fe, Al, and Si were not detected, so we derive 3σ upper limits to their abundances. The resulting elemental abundances are shown in Fig. 1A and Table S1. In defiance of dust evolution model predictions, all elements are depleted with respect to the sun; however, the volatile species are depleted by at most a factor of 100, while the refractory elements are depleted by four to five orders of magnitude. Primary atmospheres accreted from this gas cannot explain enhanced giant planet atmospheric abundances.

The bulk atomic composition of solids left behind in TW Hya is show in Fig. 1B to be nearly solar; we compare them with the composition of solar system bodies, e.g. bulk Earth *(17)*, CI chondrites *(18)*, comet 67P *(19, 20)*, and ultra-carbonaceous Antarctic micro-meteorites (UCAMMs, *21, 22*). Chondrites are a good fit to the refractory, semi-volatile elements, and S. However, they underfit TW Hya's C, N, and O abundances. Comet 67P and the UCAMMs are more abundant in these elements, so we fit a linear combination of all three bodies to the C, N, and O abundances (Fig. 1B, inset). Without UCAMMs, N is underfit by a factor of 6.5, while O is overfit by a factor of 1.4, both statistically significant. Without 67P, O is underfit by a factor of 1.8, also significant and indicative of the critical role played by cometary water ice in the oxygen budget.

Combining all three bodies matches the TW Hya solid abundances within the uncertainties of the solar system body abundances and these data. We find that ~80% of carbon and 90% of nitrogen in TW Hya's sequestered solids are locked up in UCAMM-like material (Table 1). Conversely, 56% of oxygen is locked in chondritic grains, with half of the remainder as water ice in cometary material. The O budget is clearly dominated by refractory materials, but the refractory fraction for C and N depends heavily on how one classifies UCAMMs. Obviously their survival of atmospheric entry to Earth indicates that the remaining material is refractory, but they are thought to arise through extensive radiation of C and N-rich ices on the surfaces of KBOs, which would argue in favor of a volatile classification.

If we assume that the chondritic, cometary, and UCAMM-like material are in locations analogous to our solar system, then our results are consistent with solid locking at multiple locations within the disk, both interior and exterior to the water and CO snowlines. Carbon- and nitrogen-rich material piles up outside of the CO and N_2 snowlines, which are located at 21 AU *(14, 23)* and 38 AU, corresponding to the location of TW Hya's outer rings (Figure 2A) *(24, 25).* This locked material could represent millimeter-sized grains trapped in the pressure maxima created at the inner edge of each ring, without requiring planetesimal formation. Likewise, oxygen in chondritic material could be associated with either the trap at the outer edge of the gap at 1.5 AU or the unresolved inner disk from 0.3 - 0.5 AU *(26)*. However, the cometary material, which contains 39.3% of the total locked oxygen, is not associated with any observed pressure maxima or gaps. The observed water snowline (4 AU, *27)* is well behind the inner edge of the main disk. Therefore this material must be prevented by some other mechanism, such as growth to planetesimal sizes, from drifting across the water snowline. These results suggest that dust locking in rings or large bodies efficiently prevents inner disk volatile replenishment by transported solids.

As a check on the refractory fractions, we calculate the locking efficiency of carbonaceous solids by an analytic method [see supplemental materials]. Dividing the disk into three zones at the CO snowline and dust inner rim (Fig. 3), we take representative CO/H_2 averages of 50 and 100 in zones 2 and 1, respectively, from spatially resolved ALMA observations *(9)* and convert them to C/H by assuming that all of the gas phase C is in CO. Comparing these to the carbon abundance in zone 3 allows us to determine what fraction of the initial carbon mass remains locked into the disk solids, and whether it is locked primarily in zone 1 or zone 2. Assuming the carbon present in the UCAMMs counts entirely towards the refractory fraction, we have a carbon refractory fraction of 0.98, and locking efficiencies of 0.749 and 0.249 in zones 1 and 2, respectively. If instead one assumes the carbon refractory fraction of 0.83 observed in comet 67P *(20)*, then the zone 1 locking efficiency increases to 0.97, at the expense of zone 2, 0.027. If we assume the carbon locking efficiency of 0.806, found from the earlier three-body combination fit, then only 0.2% of carbon is accreted onto the star and the solid refractory fraction is 0.974. This high value could be due to the age of TW Hya; if an earlier generation of icier solids had drifted past the CO snowline, then the settling of small, ice-free grains to the midplane would enhance the refractory fraction of the midplane solids at later times. This scenario could be tested by comparing present day stellar abundances with the assumed input abundances for the outer disk.

To summarize, we piloted a novel method to determine the bulk atomic composition of unseen solids locked at the midplanes of protoplanetary disks, using the TW Hya disk. Comparing the abundances of these solids with those of solar system bodies reveals that a combination of chondritic, cometary, and ultra-carbonaceous materials is necessary to reproduce our results. Carbon and nitrogen are mostly locked in dust traps at the inner edges of the submillimeter rings beyond 20 AU, and a majority of oxygen is likewise locked in dry silicates at the ring edges between 0.3 and 2 AU. However, a quarter of the total oxygen budget may be locked in icy planetesimals, instead of dust traps, beyond the water ice snowline at 4 AU. Locking of solids chemically isolates the inner disk, preventing replenishment of refractory carbon and water. These results suggest that any terrestrial planets forming in TW Hya from the remaining solids will be relatively 'dry' and carbon-poor, similar to those in our solar system.

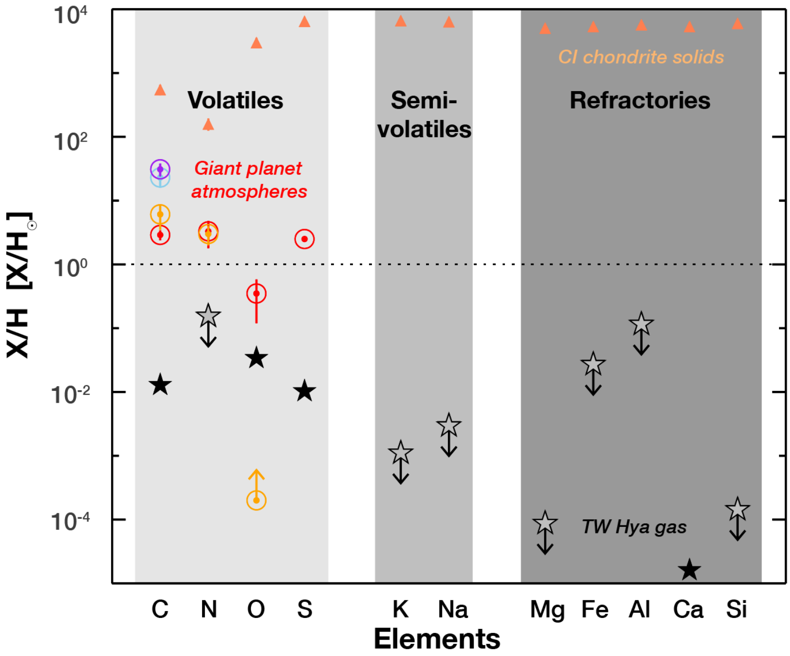

Fig. 1. Comparison of bulk elemental gas abundances: gas inside TW Hya's dust sublimation rim (black stars, gray stars with arrows for upper limits), atmospheres of *(4)*, Jupiter (red circles), Saturn (orange circles), Uranus (light blue circle), and Neptune (purple circle), and CI chondrite solids (*18*, salmon triangles). All data is plotted with error bars, which are smaller than the symbols for the most part. Abundances are normalized to the solar abundances *(3)*, with the solar value indicated by the dotted horizontal line.

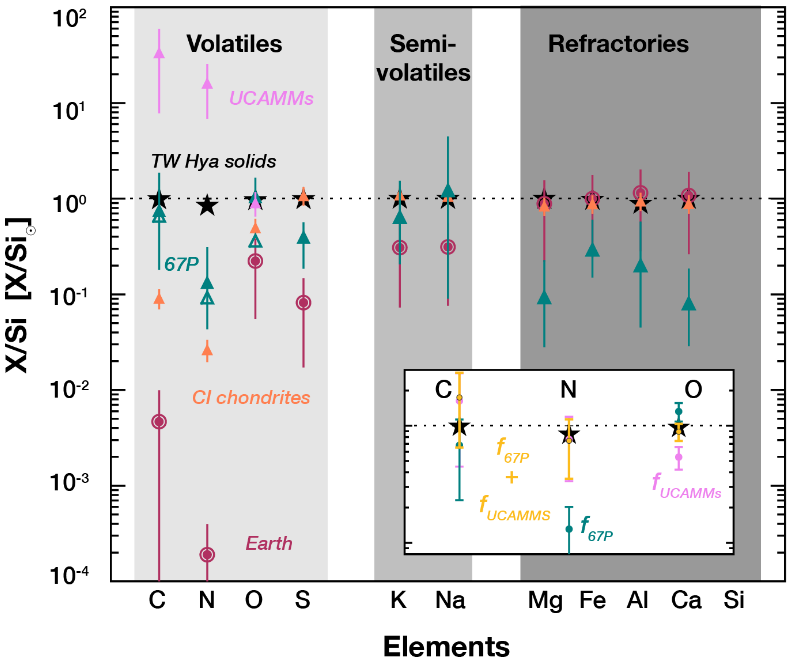

Fig. 2. Comparison of bulk elemental abundances of solids for: TW Hya (black stars), bulk Earth (core+mantle concordance model, maroon circles)*(17)*, CI chondrites (salmon triangles)*(18)*, comet 67P (bulk, dust/ice ~ 1, teal triangles) *(19, 20)*, and UCAMMs (violet triangles) *(21, 22)*. **(Inset)** Comparison of linear combinations of CI chondrites (factor 1) plus solids from a) comet 67P only (green circles, factor 0.78), UCAMMs only (violet circles, factor 0.046), and both 67P and UCAMMs (gold circles, factors 0.33, 0.042, respectively) to the C, N, and O abundances for TW Hya.

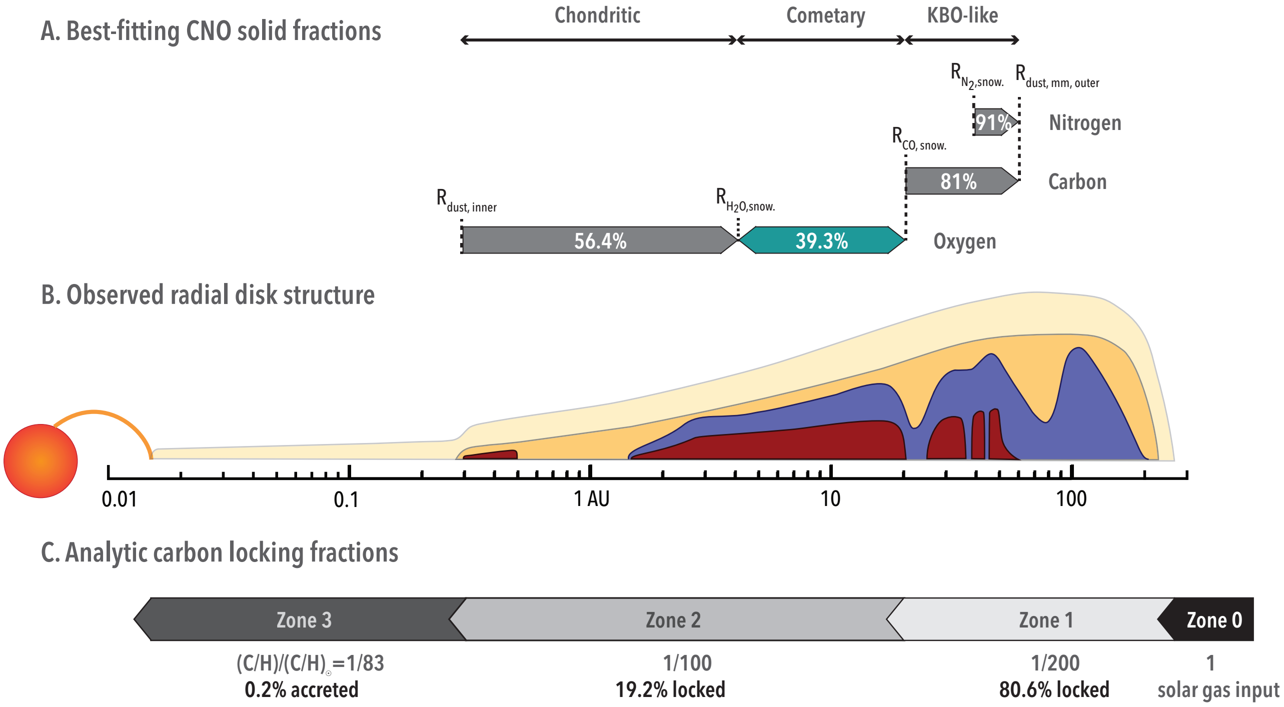

Fig. 3. (A) Dominant locking locations for C, N, and O, relative to innermost dust radius (0.3 AU) *(26)*, water ice snowline (4 AU)*(27)*, CO snowline *(14)*, and theoretical N_2 snowline. **(B) Cartoon of observed disk structures.** Millimeter grains (maroon fill, ALMA) *(24)*, small grains (purple fill, SPHERE) *(25)*, and CO gas (mustard fill) *(28, 29)*. **(C) Visualization of the analytic locking model zones.** C/H depletion factors and fraction locked or accreted are indicated, for a refractory fraction of 97.4%.

Body	**C %**	**N%**	**O%**
Chondritic	5.2	3.5	56.4
Cometary (ref)	12.2	4.0	13.3
Cometary (vol)	2.0	1.9	26.0
UCAMM-like	80.6	90.6	4.3
Bulk refractory %	$17.4 < x \leq 98$	$7.5 < x \leq 98.1$	$69.7 < x \leq 74$

Table 1. Distribution of locked C, N, and O between chondritic, cometary, and UCAMM-like material, from best-fit model in Fig. 2 inset.

References and Notes:

(1) N. Madhusudhan 2012, ApJ, 758, 36

(2) E. Bergin et al. 2015, PNAS, 112, 8965

(3) M. Asplund et al. 2009, ARA&A, 47, 481

(4) T. Owen & T. Encrenaz 2003, SSRv, 106, 121

(5) F. Du et al. 2015, ApJ, 807, 32

(6) S. Krijt et al. 2018, ApJ, 864, 78

(7) D. Anderson et al. 2017, ApJ, 845, 13

(8) L. Klarmann et al. 2018, A&A, 618, 1

(9) E. Bergin et al. 2013, Nature, 493, 644

(10) K. Schwarz et al. 2016, ApJ, 823, 91

(11) M. Kama et al. 2016, A&A, 592, A83

(12) K. Zhang et al. 2019, ApJ, in press

(13) M. Hogerheijde et al. 2011, Science, 334, 338

(14) K. Zhang et al. 2017, Nature Astronomy, 1, 0130

(15) M. McClure 2019, A&A, in press

(16) G. Ferland et al. 2017, Rev. Mexicana Astron. Astrofis., 53, 385

(17) H. Wang et al. 2018, Icarus, 299, 460

(18) K. Lodders 2010, ASSP, 16, 379

(19) A. Bardyn et al. 2017, MNRAS, 469, 712

(20) M. Rubin et al. 2019, MNRAS, 489, 594

(21) E. Dartois et al. 2017, A&A, 599, A130

(22) J. Mathurin et al. 2019, A&A, 622, 160

(23) Astronomical Unit (AU), the mean distance from Earth to the Sun, or 1.49598×10^{11} m.

(24) S. Andrews et al. 2016, ApJ, 820, 40

(25) R. van Boekel et al. 2017, ApJ, 837, 132

(26) J. Menu et al. 2014, A&A, 564, 93

(27) K. Zhang et al. 2013, ApJ, 766, 82

(28) A. Banzatti & K. M. Pontoppidan 2015, ApJ, 809, 167

(29) J. Huang et al. 2018, ApJ, 852, 122

Acknowledgments

Funding: This publication is part of a project that has received funding from the European Union's Horizon 2020 research and innovation program under the Marie Skłodowska-Curie grant agreement ICED No 749864. **Authors' contributions:** M. McClure was the lead for funding acquisition, conceptualization, data curation, methodology, formal analysis, investigation, project administration, software, visualization, and writing of the original draft. C. Dominik shared responsibility for the funding acquisition, supervision, modeling methodology, validation, and reviewing and editing. **Competing interests:** The authors have no competing interests to declare. **Data and materials availability:** All data is available in the supplementary materials, public archives, or by reasonable request to the corresponding author.

Supplementary Materials

Materials and Methods

Table S1 – S2

Fig S1 – S4

References (30 – 39)

Supplementary Materials for

Measuring the atomic composition of planetary building blocks.

Melissa K. McClure, Carsten Dominik

Correspondence to: melissa.k.mcclure@gmail.com

This PDF file includes:

Materials and Methods

Observational details

We observed TW Hya with the FIRE spectrograph (30) at the twin Magellan telescopes on January 2nd, 2013, through the University of Michigan time allocation. Two 6.0 second exposures in the Fowler 1 read mode were obtained with the 0.6" slit (R ~ 6000) under 0.45" seeing at airmass 1.009 in excellent conditions. We obtained the usual suite of arc lamp and flat-field calibrations and extracted the FIRE spectrum using the standard FIREhose pipeline, with MCN 7202 as the telluric calibrator star. The archival 2010 spectra were obtained with VLT X-shooter (31) on April 7th and May 3rd, 2010 with R~11,000 (near-IR arm: 1 - 2.5 μm) and R~18,000 (visible arm: 0.8 - 1 μm) for both epochs. We downloaded the Phase 3 data from ESO's reduced spectral database and removed the telluric absorption using the MolecFit software package. Spectra from all three epochs were corrected for their heliocentric velocities, and the X-Shooter spectra were convolved down to the resolution of the FIRE spectrum. All three epochs show H, He, Ca^{+1}, and O^0 emission lines. In the 2013 spectrum, these lines were brighter and showed additional emission from C^0 and S^0 lines at 1.07 and 1.045 μm, respectively, as shown in Figures S1-3.

Determination of n_H

Recently, these atomic carbon emission lines were shown to originate inside the dust sublimation radius in a sample of T Tauri stars with full disks and used to determine their neutral carbon column densities (15). That work provided a conversion of N_C to C/H, but did not provide a way to measure N_H directly, or measure other critical elements, e.g. O or Si. Atomic hydrogen is easy to detect in the near-infrared through the Paschen (Pa) and Brackett (Br) recombination emission line series.

Traditionally, in T Tauri stars these lines were interpreted as arising in a combination of the magnetospheric accretion columns connecting the inner, gaseous disk to the stellar photosphere and stellar winds, with a wide range of temperatures and densities *(32)*. For TW Hya using the full line fluxes of the Pa and Br series, electron densities and temperatures of $n_e \sim 10^{12}$ - 10^{13} cm^{-3}, corresponding to $N_H \sim 3.4\times10^{20}$ - 9.1×10^{21} cm^{-2}, have been inferred for the stellar accretion shock *(33)*. However, recent interferometric observations of disks have shown that the emitting region of these lines extends into the inner 0.1 AU of disks around T Tauri stars *(34)*. If one could kinematically isolate the inner disk component from that of the accretion columns, then N_H could be directly compared with N_C.

We took advantage of the multi-epoch observations to explore changes to the H^0 emission line morphology using time differential spectroscopy. Using an existing sigma-clipping LOESS fitting script *(35)*, we determined, and subtracted off, the continuum under the lines of interest in each spectrum. For the Ca^{+1} , O^0 , C^0 and S^0 lines, we integrated the spectra over the blended lines and list the fluxes in Table S1. For the non-detected strong lines, we integrated over the continuum rms value to obtain 3σ upper limits. The hydrogen lines required special treatment to kinematically isolate the inner disk emission. In Fig. S3A, we show the local continuum subtracted spectra around the H^0 Paschen γ line for the 2010b and 2013 epochs in velocity space. Both emission lines are centered around the stellar rest velocity, with the 2013 spectrum as the stronger of the two, and both clearly have structure in their wings. The 2013-2010b subtraction residuals reveal this structure to be an inverse P-Cygni profile, with peak emission at -143 km/s and absorption at +124 km/s, consistent with expected velocities for the stellar magnetospheric accretion columns *(36)*. The strengthening of these features is indicative of more material in the accretion flow onto the central star in the 2013 epoch.

The scenario laid out by the changes in the emission lines is shown on the right hand side of Fig. S3. In both epochs of 2010, TW Hya was accreting mass from the disk at a nominal rate. However, in 2013, a ring of denser material was accreted, strengthening the existing emission lines and revealing weak lines of C^0 and S^0. Subtracting the 2010b spectrum should remove the contribution of the star, chromosphere, and bulk disk to the emission lines in the 2013 spectrum, effectively isolating the emission from the accretion columns and the inner disk. By fitting-out the accretion columns' inverse P-Cgyni signature from the hydrogen lines, we obtain the integrated fluxes of the hydrogen line components for only the inner disk. Ratios between the hydrogen lines fluxes, Paβ/Paγ, varied from 2.3 in 2010 to 2.7 in 2013. Comparison with a chemical model can yield direct constraints on n_H, as described below.

Chemistry and radiative transfer model

We constructed a slab model of the overdensity in the inner disk and calculated the emergent flux density ratios for a grid of n_H and atomic abundances using version 17.02 of the photo-ionization code Cloudy *(16)*. This code also includes a chemical network with atomic and molecular opacities appropriate to the hot, dense, dust-free region interior to the inner dust rim, which enables the radiative transfer calculation in the absence of dust opacity. As in our previous work with carbon line emission *(15)*, we enabled the larger H_2 molecule module in Cloudy *(37)*, as the physics and chemistry of molecular hydrogen is critical at these small radii.

The slab was heated by a combination of irradiation and viscous dissipation. We created a composite radiation field from ATLAS9 stellar models with solar metallicity *(38)* at the stellar effective temperature and luminosity, $T_{\rm eff}$, = 3850 K with $L_{\rm star}$ = 0.3 $L_{\rm sol}$, and the stellar accretion shock temperature and luminosity, $T_{\rm shock}$ = 8000 K with $L_{\rm shock}$ = 0.01. There is an additional contribution to the radiation field from X-rays, assuming a 10 MK bremsstrahlung emission spectrum, with a luminosity of $L_X=10^{30}$ erg/s between 0.3 keV and 10 keV *(39)*. Accretion heating was enabled using the Hextra keyword, assuming an α of 0.01, the stellar mass $M_{\rm star}$, and a radius half-way through the slab. The slab extended from the assumed disk co-rotational radius at 3 stellar radii ($R_{\rm star}$ = 1.1 $R_\odot$) out to 0.024 AU, with a radially dependent power-law hydrogen density of power -2. We chose the outer radius of the slab to be the size corresponding to the distance over which gas would viscously accrete in the TW Hya system on the timescale between the 2013 and 2010 epochs.

The hydrogen flux ratios produced by the model indicate an increase from log (n_H) = 14.2 to log (n_H) = 14.55 between 2010 and 2013, consistent with scenario sketched in Fig. S3C. We assume that the presence of weak C^0 and S^0 features in the 2013 spectrum is an indication of a minimum density needed to see them, rather than a change in their abundance relative to H during this time. At these densities, the main 'ionization' process for hydrogen is through charge exchange collisions with sulphur. To determine X/H for a variety of elements, we first determined S/H from the observed blended S^0/Paγ flux ratio, confirmed that the Paβ/Paγ ratio was still valid, and then fit the remaining X/H in order of most decreasing solar abundance, checking that the Paβ/Paγ ratio remained within the observed uncertainties. The resulting abundances are given in the last column of Table S1 and visually in Fig. S4, and the analysis is conducted in the Main Text.

Radial lock-out toy model

As an independent check on the location where carbon is locked out of the accreting gas, we formulate a toy model. We define the model as a parcel of gas that initially sits in the outer disk but is radially transported via accretion processes through the disk to the launching region for the stellar magnetospheric accretion columns. The parcel has an initial gaseous carbon mass $M_{g,0}$, from which solid carbon condenses out with mass $M_{d,1} = M_{g,0} - M_{g,1}$, leaving a depleted carbon gas mass of $M_{g,1}$. The solid carbon component can be split into dust that is more refractory than CO, with fraction f_r, and volatile dust in the form of CO. The grains are assumed to move radially along with the gas, unless it is locked out of the accretion stream. This locking could be caused either by the gas decoupling and entrapment of larger, millimeter-sized dust grains at pressure maxima or by the formation of bodies that are large enough to neither accrete with the gas nor radially drift. The model is agnostic to the exact locking mechanism. We do not consider complications from decoupling of the gas and non-locked dust due to radial drift; we assume that this dust simply moves with the gas. We define a fraction of the dust, $f_{L,1}$, that is locked in some manner, while the remaining dust exists in small, coupled grains that accrete with the gas across the CO snowline. The successfully transported dust is defined as:

$$M_{d,d,1} = (1 - f_{L,1})M_{d,1}$$

At this point the volatile dust sublimates, releasing carbon back into the gas phase. Therefore the new carbon gas mass is:

$$M_{g,2} = M_{g,1} + (1 - f_r)M_{d,d,1}$$

$$= M_{g,1} + (1 - f_r)(1 - f_{L,1})M_{d,1}$$

$$= M_{g,1} + (1 - f_r)(1 - f_{L,1})(M_{g,0} - M_{g,1})$$

Solving for the locking fraction in zone 1, $f_{L,1}$, yields:

$$\frac{M_{g,2} - M_{g,1}}{M_{g,0} - M_{g,1}} = (1 - f_{L,1})(1 - f_r)$$

$$f_{L,1} = 1 - \frac{1}{1 - f_r} \cdot \frac{M_{g,2} - M_{g,1}}{M_{g,0} - M_{g,1}}$$

$$= 1 - \frac{1}{1 - f_r} \cdot \frac{X_{g,2} - X_{g,1}}{X_{g,0} - X_{g,1}}$$

where X is the C/H abundance, assuming that no appreciable hydrogen mass is locked into the grains. The dust mass interior to the CO snowline is then the fraction of the transported dust that is more refractory than CO:

$$M_{d,2} = f_r M_{d,d,1}$$

A fraction of this more refractory dust, $f_{L,2}$, is also locked eventually, either through growth to large grains or to planetesimal sizes. Therefore, the mass of dust that is transported across the inner dust rim is the dust mass in zone 2 less the fraction locked there:

$$M_{d,d,2} = (1 - f_{L,2})M_{d,2}$$

and the mass of gas phase carbon interior to the innermost dust rim is then the carbon gas mass of zone 2, with the addition of the mass of refractory transported dust, which sublimates.

$$M_{g,3} = M_{g,2} + M_{d,d,2}$$

$$= M_{g,2} + (1 - f_{L,2})M_{d,2}$$

$$= M_{g,2} + (1 - f_{L,2}) f_r M_{d,d,1}$$

$$= M_{g,2} + (1 - f_{L,2}) f_r (1 - f_{L,1}) M_{d,1}$$

$$= M_{g,2} + (1 - f_{L,2}) f_r (1 - f_{L,1}) (M_{g,0} - M_{g,1})$$

Solving for the locking fraction in zone 2, $f_{L,2}$, yields:

$$\frac{M_{g,3} - M_{g,2}}{M_{g,0} - M_{g,1}} = (1 - f_{L,2})(1 - f_{L,1}) f_r$$

$$f_{L,2} = 1 - \frac{1}{(1 - f_{L,1}) f_r} \cdot \frac{M_{g,3} - M_{g,2}}{M_{g,0} - M_{g,1}}$$

$$= 1 - \frac{1}{(1 - f_{L,1}) f_r} \cdot \frac{X_{g,3} - X_{g,2}}{X_{g,0} - X_{g,1}}$$

We cannot simultaneously constrain both the locking fraction and refractory fraction, but if we assume a refractory fraction, either from the radial C abundance estimates in the Main Text or from comet 67P, and solar abundances for $M_{g,0}$, then we can use the three observed X = C/H values to solve for the locking fractions interior and exterior to the CO snowline.

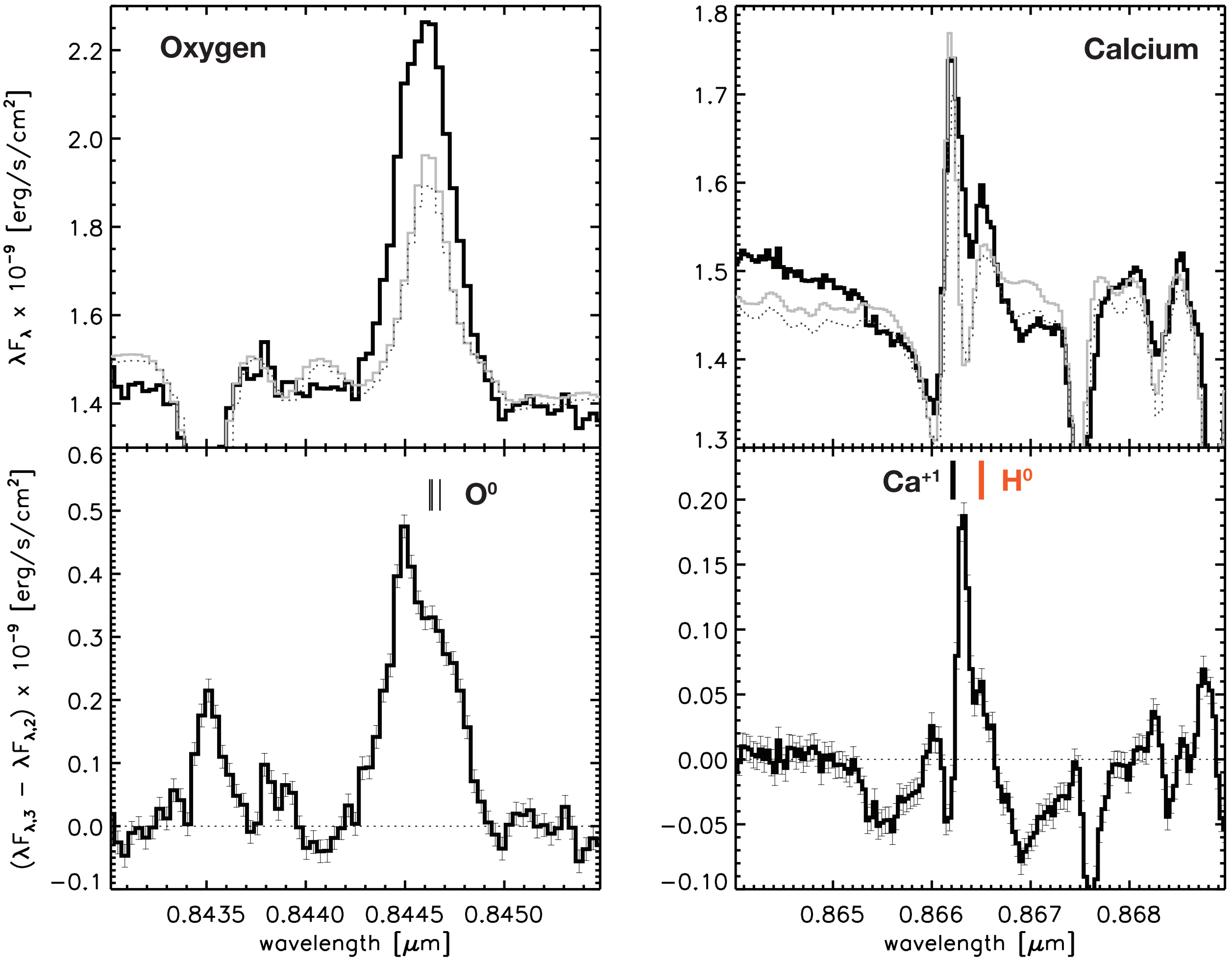

Fig. S1.

Top: Comparison of the three observed epochs of TW Hya: 2010a (gray, dotted line), 2010b (gray, solid line), and 2013 (black, thick line). The oxygen line (left) is a triple line blend, and the calcium line (right) is blended with an H^0 Paschen series line and an absorption artifact from the telluric correction of that line, which we fit out before determining the integrated flux. Bottom: Residual spectra after subtraction of epoch 2 from epoch 3.

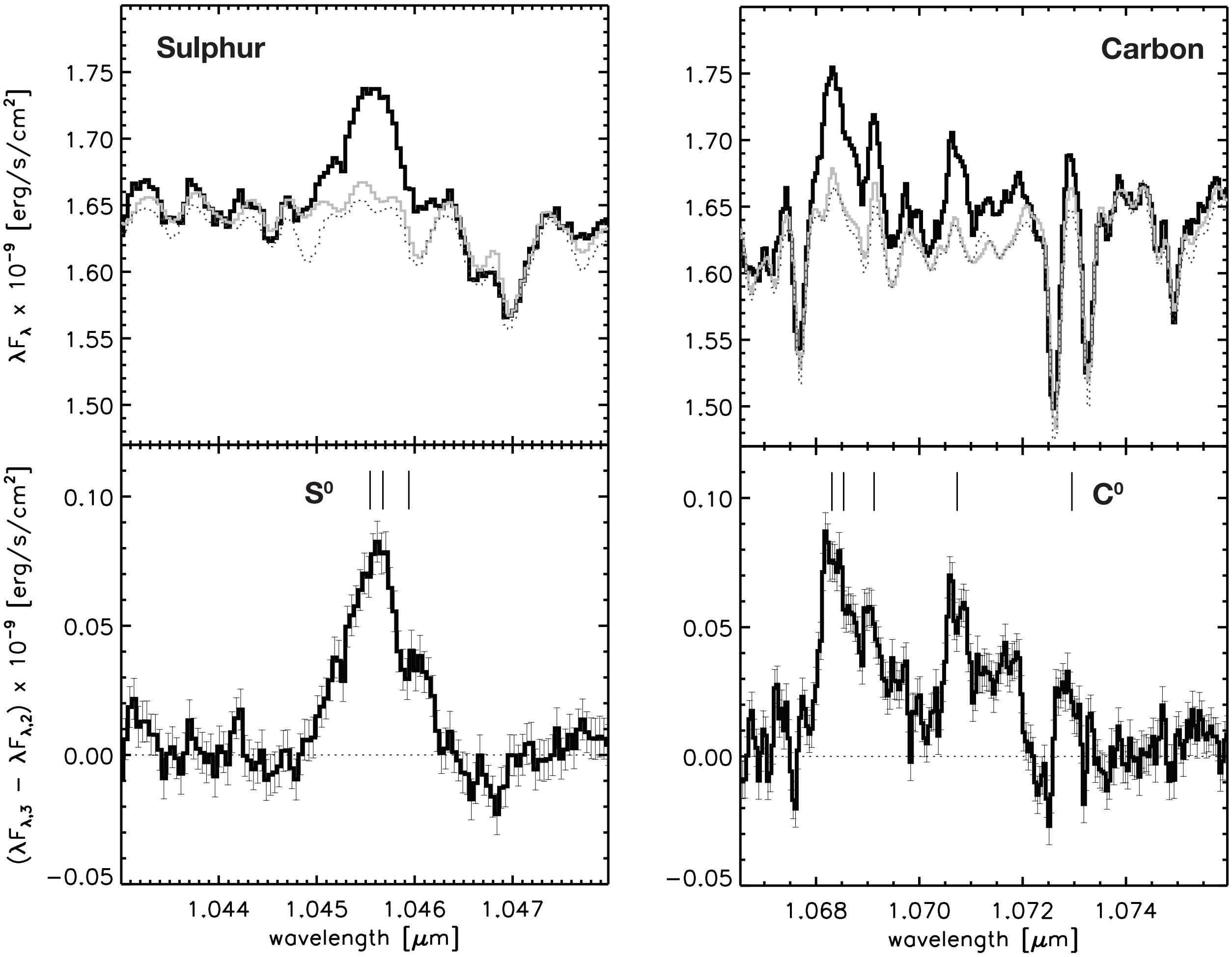

Fig. S2.

The same as Fig. S1, but for sulphur (left) and carbon (right). The integrated flux of the sulphur line is includes the three-line blend, while the carbon flux includes only the first three lines. Line styles are the same as in Fig. S1.

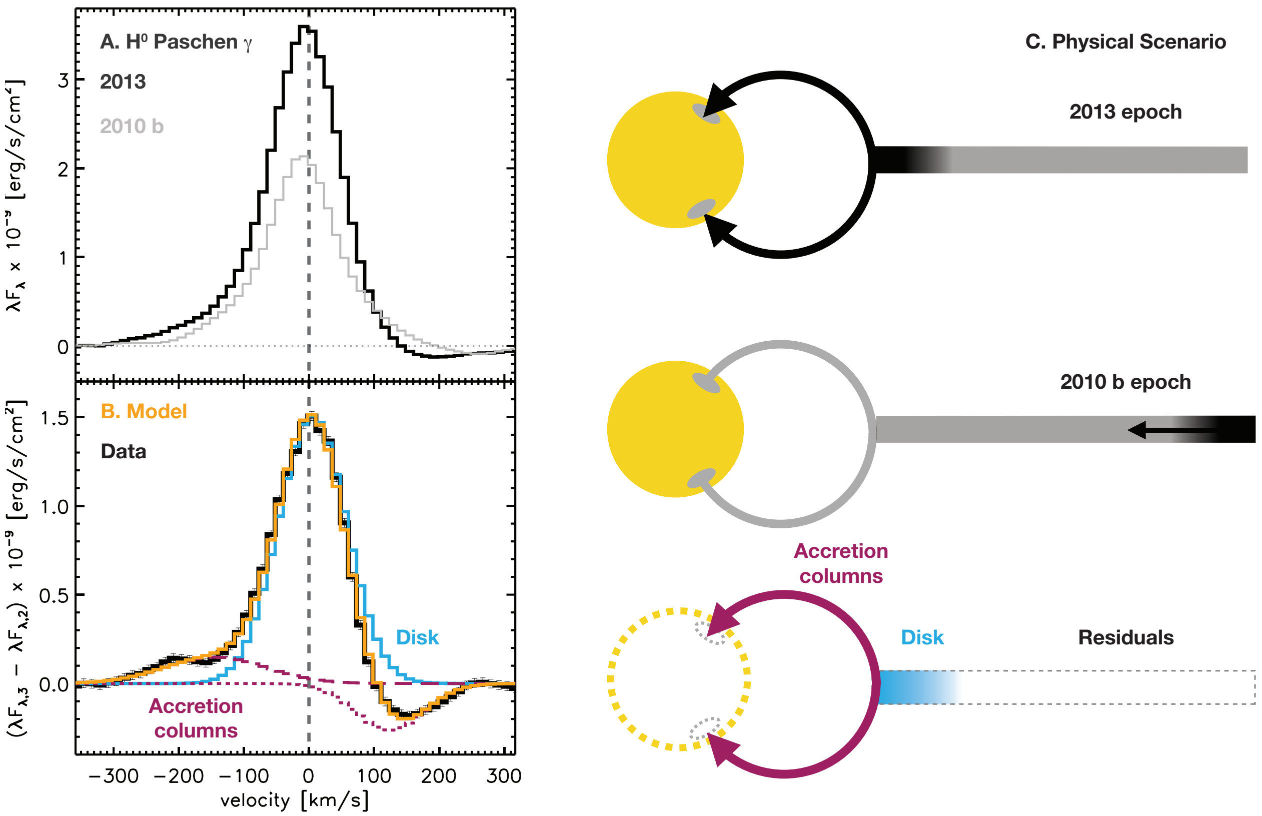

Fig. S3.

A. Comparison of the Paγ line emission for the 2010b epoch (gray line) and 2013 epoch (black line) after continuum subtraction. Dashed vertical line indicates the local stellar velocity, to which the spectra have been corrected. B. Gaussian decomposition of the residual spectrum of 2013-2010b. Model components include the accretion columns (purple) and inner disk (cyan). The total fit (yellow) is shown against the data (black). C. Cartoon of the physical scenario revealed by the time differential spectroscopy. The contribution from the star (yellow) and cooler disk (gray) are removed by subtraction of the weak accretion epoch, allowing isolation of the inner disk emission after removing the accretion column contribution, as in panel B.

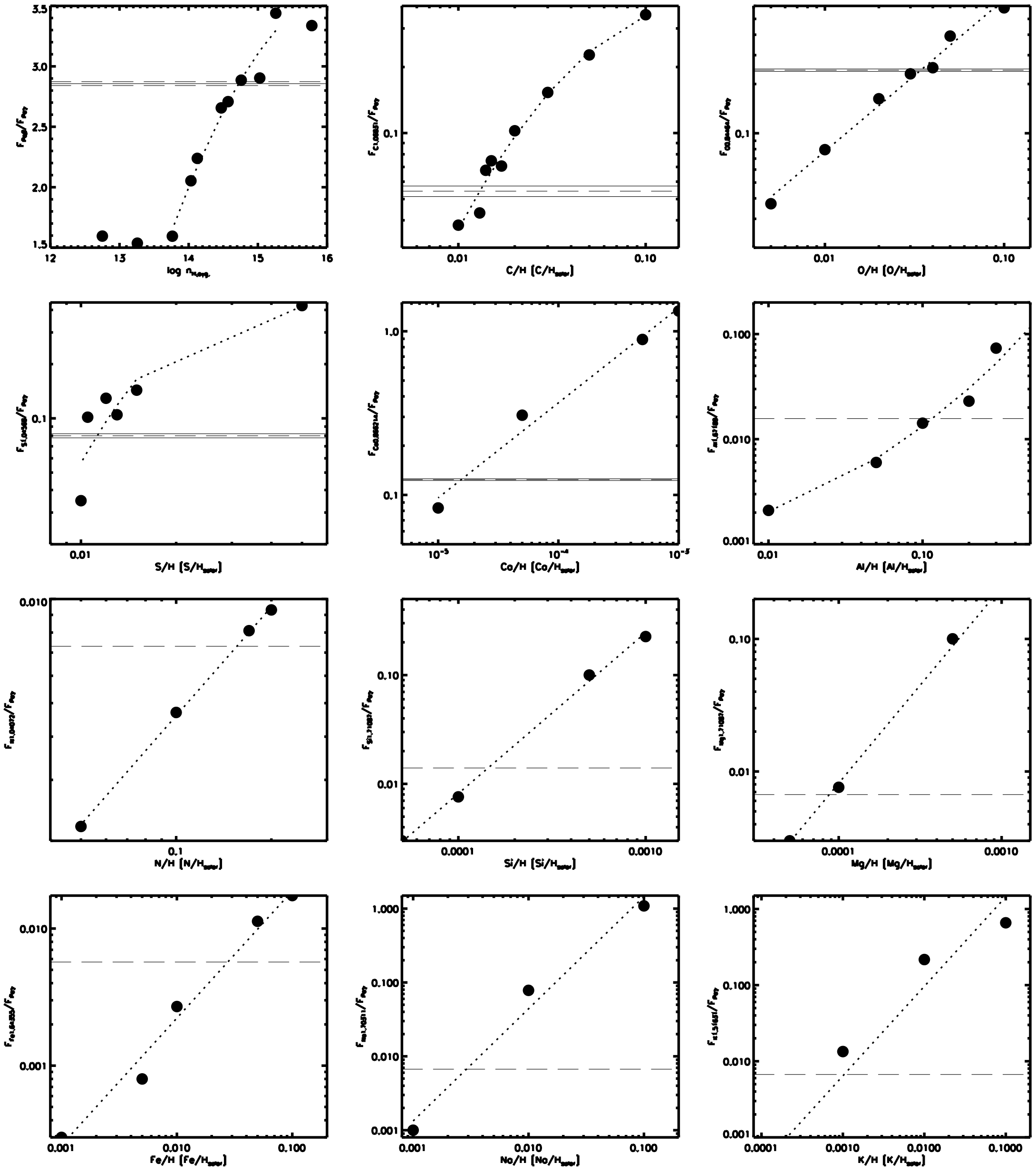

Fig. S4.

(Upper left corner): Flux ratios between Paβ and Paγ, versus n_H. (Rest): Flux ratios relative to Paγ versus abundance relative to H in solar units for all elements in this study. Error bars are indicated for the fours elements with detections, and 3σ upper limits are indicated for the others.

Atomic species	**Line [μm]**	**F_{int} [erg/s/cm^2]**	**S/N (F_{int})**	**$F_X/F_{Pa\,\gamma}$**	**X/H [X/Hsolar]**
H^0	1.09381 (Pa γ)	7.0×10^{-9}	187.0	-	
H^0	1.28181 (Pa β)	2.0×10^{-8}	1090.5	2.857 ± 0.016	$\log (n_H) = 14.74 \pm 0.02$
C^0	1.06831	3.8×10^{-10}	18.3	0.0543 ± 0.0030	$C/H = 1.29\times10^{-2} \pm 3.69\times10^{-4}$
S^0	1.04568 blend	5.6×10^{-10}	39.8	0.0800 ± 0.0021	$S/H = 1.03\times10^{-2} \pm 9.12\times10^{-5}$
O^0	0.84464 blend	1.7×10^{-9}	58.7	0.2429 ± 0.0043	$O/H = 3.41\times10^{-2} \pm 6.43\times10^{-4}$
Ca^{+1}	0.866214	8.7×10^{-10}	93.1	0.1240 ± 0.0015	$Ca/H=1.61\times10^{-5} \pm 3.30\times10^{-7}$
Al^0	1.67189	$< 1.1\times10^{-10}$	1	< 0.0157	$Al/H < 1.16\times10^{-1}$
N^0	1.04072 blend	$< 2.5\times10^{-10}$	1	< 0.0073	$N/H < 1.55\times10^{-1}$
Si^0	1.58884	$< 9.8\times10^{-11}$	1	< 0.0140	$Si/H < 1.44\times10^{-4}$
Fe^{+1}	1.64355	$< 4.0\times10^{-11}$	1	< 0.0057	$Fe/H < 2.72\times10^{-2}$
Mg^0	1.71087	$< 4.7\times10^{-11}$	1	< 0.0067	$Mg/H < 8.77\times10^{-5}$
Na^0	1.70311	$< 4.7\times10^{-11}$	1	< 0.0067	$Na/H < 2.97\times10^{-3}$
K^0	1.51631	$< 4.7\times10^{-11}$	1	< 0.0067	$K/H < 1.11\times10^{-3}$

Table S1.

Observed atomic emission lines, integrated fluxes, and fitted abundances for the slab model.

Parameter	Value	Reference
Stellar and accretion properties		
T_{eff}	3800 K	Sokal et al. (2018)
L_{star}	0.3 $L_\odot$	Ingleby et al. (2013)
M_{star}	0.8 $M_\odot$	Ingleby et al. (2013)
R_{star}	1.1 $R_\odot$	Ingleby et al. (2013)
L_{shock}	0.01 $L_\odot$	Ingleby et al. (2013)
T_{shock}	8000 K	assumed
Inner disk slab		
R_{in}	0.015 AU	assumed, corot. radius
R_{out}	0.024 AU	assumed, time cadence
log ($n_{H,0}$)	14.75 cm^{-3}	fitted
power	-2	assumed, McClure (2019)

Table S2.

Physical model for the innermost disk of TW Hya

References

(30) R. Simcoe et al. 2013, PASP, 125, 270

(31) J. Vernet et al. 2011, A&A, 536, 105

(32) S. Edwards et al. 2013, ApJ, 778, 148

(33) W. Vacca & G. Sandell 2011, ApJ, 732, 8

(34) J. Eisner et al. 2014, MNRAS, 443, 1916

(35) M. McClure et al. 2013, ApJ, 769, 73

(36) L. Hartmann et al. 2016, ARA&A, 54, 135

(37) G. Shaw et al. 2005, ApJ, 624, 794

(38) F. Castelli & R. Kurucz 2003, IAUS, 210P, A20

(39) C. Rab et al. 2018, A&A, 609, 91